This is a previous version of the article published in Colloids and Surfaces A: Physicochemical and Engineering Aspects. 2021, 613: 126060.
https://doi.org/10.1016/j.colsurfa.2020.126060

Copper ferrite nanospheres composites mixed with carbon black to boost the oxygen reduction reaction

J.X. Flores-Lasluisa[1], D. Salinas-Torres[1], M.V. López-Ramón[2], M.A. Álvarez[2], C. Moreno-Castilla[3], D. Cazorla-Amorós[4], E. Morallón[1,*,&]

[1]Departamento de Química Física e Instituto Universitario de Materiales, Universidad de Alicante, Ap. 99, E-03080, Alicante, Spain

[2]Departamento de Química Inorgánica y Orgánica, Facultad de Ciencias Experimentales, Universidad de Jaen, E-23071 Jaen, Spain

[3]Departamento de Química Inorgánica, Facultad de Ciencias, Universidad de Granada, E-18071 Granada, Spain

[4]Departamento de Química Inorgánica e Instituto Universitario de Materiales, Universidad de Alicante, Ap. 99, E-03080, Alicante, Spain

***Corresponding Author*:** Emilia Morallón, morallon@ua.es

& This paper is dedicated to the memory of our friend the late Prof. Francisco Rodríguez-Reinoso.

Abstract

Copper ferrite nanospheres (CFNS) were prepared by a solvothermal method and they were calcined at different temperatures ranging from 200-600 ºC, resulting in CFNS-based materials with different both surface chemistry and structural features, which play a crucial role in the electrocatalytic activity of carbon black-containing CFNS catalysts towards the oxygen reduction reaction (ORR). The study was addressed to elucidate which kind of crystalline phases, as well as surface chemistry of CFNS were responsible for enhancing the electrocatalytic activity in ORR. The pristine CFNS and CFNS200 (calcined at 200 ºC) exhibited cubic spinel, cuprite and copper as main crystalline phases. In the case of CFNS400, it also displays the cubic phase along with a new phase (tenorite). Apart from the tenorite, CFNS600 exhibited hematite, and the cubic phase of spinel shifted to the tetragonal phase. Regarding the electrocatalytic activity in ORR, the CFNS revealed poor activities compared to those of carbon black-containing CFNS catalysts. The high-performing catalyst was CFNS400/Vulcan in terms of current density and onset potential along with its good stability. This improvement may be assigned to both the chemical composition and structure.

Keywords: Copper ferrite, nanosphere composites, electrocatalyst, oxygen reduction reaction

1. Introduction

The development of clean and sustainable energy sources has recently increased to face the depletion of fossil fuels and their associated environmental concerns [1]. Fuel cells and metal-air batteries are promising devices that meet future energy requirements. However, the oxygen reduction reaction (ORR) that occurs in the cathode exhibits sluggish kinetics, and thus, efficient catalysts are needed [2,3]. Platinum-based materials are the most active catalysts for ORR; however, like all noble metals, their cost is high and their availability is limited [4,5]. Therefore, the development of high-performing catalysts for ORR based on high abundance, low cost and environmentally friendly materials is mandatory. Materials such as nitrogen-doped carbon materials [6], metal oxides/carbon materials [7], transition metal carbide/heteroatom-doped carbon [8], and perovskites/carbon materials [9], have been extensively studied over the last years.

Among metal oxide materials, ferrites with formula AFe_2O_4 where A is a divalent cation have attracted great attention because of their tunable composition and properties. Usually, they have an inverse or mixed spinel structure formed by a cubic close-packed oxide anions array where the cations occupy the tetrahedral and octahedral sites according to the stoichiometry $[A_{1-x}^{II}B_x^{III}]^{tet}[A_x^{II}B_{2-x}^{III}]^{oct}O_4$ [10]. In the inverse spinels x = 1 and in the mixed ones 1 > x > 0. This kind of structures endow spinel-based materials with abundant octahedral edges and redox couple of both cations that can act as catalytic centres for multiple electrochemical reactions such as those involving oxygen molecule (ORR and oxygen evolution (OER)) [11,12] and hydrogen peroxide reduction [13]. Apart from multiple interesting properties, these materials exhibit redox processes that play a role in the reduction mechanism [14]. It should be noted that cobalt ferrite spinels are the most studied catalysts because of the promising performance of cobalt oxide materials for ORR [11,15]. Even though the copper ferrite spinels have not been profusely studied for this electrochemical application, the interaction Cu-Fe has been already reported to boost the ORR due to a synergetic effect between both Cu and Fe that favours the adsorption of oxygen [16]. Not only chemical composition affects the ORR performance, but the crystal phase of the spinel also has an influence as several studies have reported [17–19]. The cubic phase has shown higher activity towards ORR than the tetragonal phase because the cubic phase provides a higher number of active sites and binds oxygen more strongly [17]. However, a study on single crystal $(Mn,Co)_3O_4$ octahedral has revealed that a facet with a tetragonal structure exhibits a higher catalytic response than the cubic structure [18].

Ferrites have two important drawbacks that limit their electrocatalytic activity in ORR. On one side, they possess low electrical conductivity that hinders the electron transfer [20], and on the other side, the metal oxide powder is prone to aggregate, which decreases the number of exposed active sites for the ORR [14]. Therefore, the overcoming of these two drawbacks is necessary to enhance the performance of the ferrite oxides towards ORR. To do that, they can be incorporated into conducting materials like carbon materials. Carbon materials have high electrical conductivity, high thermal stability, high surface area, and their cost is low. In addition to the activity of carbon materials for ORR, previous studies have reported a synergetic effect between carbon materials and metal oxide materials that leads to a higher catalytic activity of the hybrid materials in ORR [21,22].

In this work, copper ferrite nanospheres (CFNS) have been studied as electrocatalysts for ORR. The CFNS were synthesized by a solvothermal method and heat-treated at different calcination temperatures to modify their physicochemical and electrochemical properties, resulting in a different electroactivity towards ORR. Especially, the crystal structure of the metal oxides plays a role in the activity, being the CFNS composites with the cubic spinel and tenorite phases the most catalytic for ORR. The CFNS oxides are mixed with Vulcan XC-72R to improve the electrocatalytic activity, resulting in materials with a good electroactivity in ORR.

2. Experimental

2.1. Synthesis procedure

The synthesis of the CFNS composite was performed by a solvothermal method described elsewhere [23–25]. Firstly, the precursors $CuCl_2 \cdot 2H_2O$ (3.13 mmol) and $FeCl_3 \cdot 6H_2O$ (6.26 mmol) were dissolved in ethylene glycol (50 mL) followed by the addition of sodium acetate (4.5 g) and polyethylene glycol (2.0 g). The solution was stirred for 30 min and then the resulted solution was transferred into a 125 mL Teflon-lined stainless-steel autoclave, which was placed in a stove at 200 ºC for 12 h before cooling to room temperature. The product was centrifuged and washed several times with ethanol and finally dried at 60 ºC for 8 h. Then, different portions of the CFNS composite were calcined in an air-oven at 200, 400, and 600 ºC for 3 h. Samples were denoted as CFNS200, CFNS400, and CFNS600, respectively.

The CFNS/Vulcan-based materials were prepared by physically mixing both materials (ratio of CFNS/Vulcan equal to 1:1) using an agate mortar until a homogenous material was formed.

2.2. Physicochemical characterization

The morphologies and microstructures of the as-synthesized samples were characterized by scanning electron microscopy (SEM, Carl Zeiss SMT, Oberkochen, Germany), and transmission electron microscopy (TEM, JEOL JEM-1010 microscope, Croissy, France). The Brunauer-Emmett-Teller (BET) surface area (S_{BET}) was determined by N_2 adsorption-desorption isotherms at -196 ºC using an Autosorb 1 from Quantachrome (Boyton Beach, FL, USA).

The surface composition of the CFNS materials was analyzed by X-ray photoelectron spectroscopy (XPS) using an Escalab 200R system (Thermo Fisher Scientific, East Grinstead, UK) equipped with MgKα X-ray source. The crystalline structure of the metal oxide materials was characterized by X-ray diffraction (XRD) using an X-ray Empyrean diffractometer with PIXcel-3D detector (Empyrean, PANanalytical, Almelo, Netherlands).

Electrical conductivity was measured by a four-probe method using a Lucas Lab equipment. To do this, disk-shaped samples were prepared by mixing CFNS samples or CFNS/Vulcan composites with the minimum amount of binder (PTFE), obtaining comparable thicknesses and the same diameter for all samples.

2.3. Electrochemical characterization

To study the electrochemical characterization of the as-synthesized materials, an ink was prepared by sonicating a suspension containing 1 mg of the CFNS or CFNS/Vulcan-based material and 1 mL of a solution (20 vol% isopropanol, 80 vol% water and 0.02 vol% Nafion®).

Electrochemical measurements were carried out in a three-electrode cell in 0.1 M KOH solution at 25 ºC using an Autolab PGSTAT302 bipotentiostat (Metrohm, Netherlands). A rotating ring-disk electrode (RRDE) from Pine Research Instruments (USA) equipped with a glassy carbon (GC) disk (5.61 mm diameter) and a Pt ring were used as working electrodes. A graphite bar was used as a counter electrode (supplied by Mersen Ibérica)

and a home-made reversible hydrogen electrode (RHE) introduced in the same electrolyte as a reference electrode. It consists of deposited platinum black on a Pt wire introduced into a Luggin, which contains the same electrolyte as the electrochemical cell (Figure S1).

To characterize the samples, cyclic voltammetry (CV) and linear sweep voltammetry (LSV) experiments were performed. The amount of sample deposited on the disk electrode was optimized to achieve a loading of 480 μg/cm^2. Firstly, to perform the CVs, N_2 was bubbled for 20 min in the electrolyte, and for CFNS samples the votammograms were obtained from -0.45 to 1 V (vs RHE), but for the CFNS/Vulcan composites, the potential limits in the CV are 0 and 1 V (vs RHE), at 50 mV s^{-1} in 0.1 KOH solution.

The electroactivity of the materials towards ORR was studied by LSV experiments using different rotation rates between 400 and 2025 rpm at 5 mV s^{-1} from 1 to 0 V (vs RHE) in O_2-saturated 0.1 M KOH solution. The Pt ring electrode was kept at 1.5 V during all the measurements. The electron transfer number (n_e^-) was calculated from the oxidation of hydrogen peroxide at the Pt ring electrode, according to the following equations [26]:

$$HO_2^-[\%] = 200x\frac{I_{ring}/N}{I_{disk}+I_{ring}/N} \qquad \text{(Eq. 1)}$$

$$n_{e^-} = \frac{4I_{disk}}{I_{disk}+I_{ring}/N} \qquad \text{(Eq. 2)}$$

where I_{disk} and I_{ring} are the currents measured at disk and ring, respectively, and N is the collection efficiency of the ring that was experimentally determined as 0.37.

The Tafel slopes were obtained from the LSV by plotting the potential versus the logarithm of the kinetic current (log j_k), at low overpotentials, that is, when the reaction is under kinetic control.

The stability test was carried out through chronoamperometric experiments with the RRDE at 1600 rpm in O_2-saturated 0.1 M KOH solution at a constant potential of 0.5 V. After 3 hours at 0.5 V, methanol was added to the background electrolyte until 1.0 M concentration was reached.

3. Results and discussion

3.1. Physicochemical characterization

The CFNS material was heat-treated at different calcination temperatures after the solvothermal process. The heat-treatment altered the physicochemical properties of the pristine material. The microstructure and the morphology of the samples were characterized by TEM and SEM techniques, respectively. Figure 1 depicted both TEM and SEM micrographs. They reveal that CFNS and CFNS200 materials are formed by numerous well-distributed heterojunction nanocrystals with a dandelion-like structure [23]. This structure is not observed in CFNS400 and CFNS600 materials because the high calcination temperature caused the sintering of the nanocrystals, smoothing the surface of the nanospheres. In addition, sintering between some nanospheres occurred at the higher calcination temperature in sample CFNS600. The size of CFNS was not affected by calcination temperatures up to 400 ºC. The average size of the nanospheres determined by measuring at least 200 particles was around at 150 nm [23]. The sintering of the nanocrystals on the surface does not affect the size of the nanospheres; however, the BET surface area from N_2 adsorption-desorption isotherms (Figure S2 in Supporting information) is reduced from 47 m^2 g^{-1} in CFNS to 38, 12, and 3 m^2 g^{-1} in CFNS200, CFNS400, and CFNS600, respectively. The shapes of the isotherms are similar to those of type II in the IUPAC classification [27], indicating non-porous or macroporous materials. All isotherms show a small hysteresis cycle with a closure point at P/P_0 around 0.45, attributable to interparticle pores.

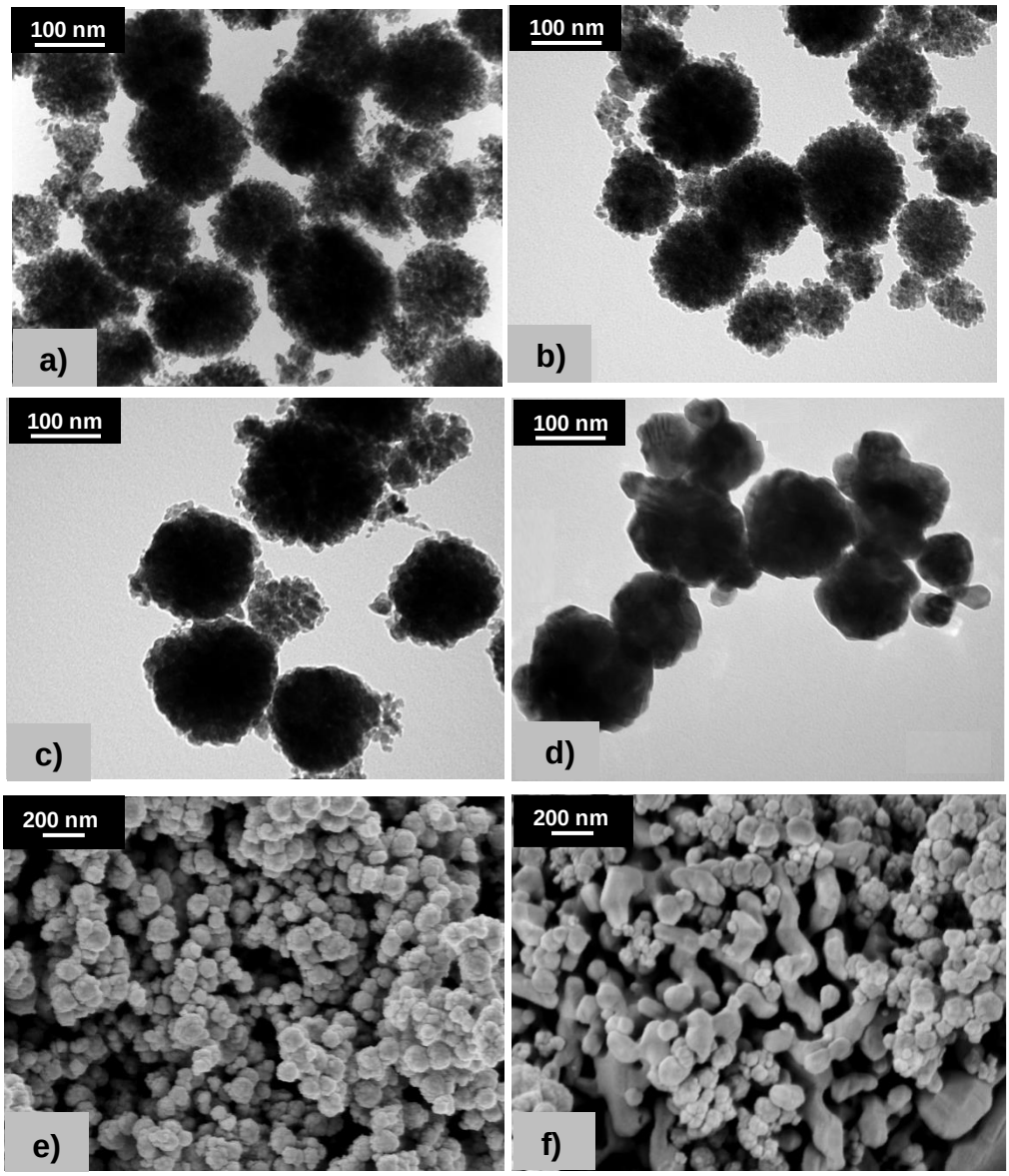

Figure 1. Transmission electron microscopy (TEM) micrographs of **(a)** CFNS; **(b)** CFNS200; **(c)** CFNS400; **(d)** CFN600 and scanning electron microscopy (SEM) micrographs of **(e)** CFNS400 and **(f)** CFNS600.

It is well known that the crystal structure of the metal oxides influences their electrocatalytic response towards ORR; thus, the materials were characterized by XRD and results obtained from the diffractograms of the samples shown in Figure S3 are compiled in Table 1. The formation of different crystal structures and their percentage was greatly influenced by the calcination temperature. The CFNS and CFNS200 have the same crystallite phases of c-$CuFe_2O_4$, Cu_2O and Cu. The presence of metallic Cu is related to the reduction of some Cu^{2+} ions present in the solution by ethylene glycol. The cuprite and the metallic copper disappear in CFNS400 due to their oxidation to tenorite. The phase percentage of c-$CuFe_2O_4$ slightly decreased from CFNS to CFNS400 but the

crystallite size remained unchanged. These results were described elsewhere [23]. CFNS600 had three phases: t-$CuFe_2O_4$, tenorite and hematite. It is well known that copper ferrite can exist in two crystallographic forms as cubic or tetragonally distorted structures, according to the concentration of distorting Jahn-Teller Cu^{2+} ions in octahedral B sites of the spinel structure [28]. The cubic structure is stable below 300 ºC and the tetragonal is stable over 400 ºC [29,30]. The phase transformation is irreversible, because of the greater thermodynamic stability of the tetragonally distorted *versus* cubic spinel [31]. The cubic-to-tetragonal transformation involves the following exchange reaction: $Fe^{3+}_B + Cu^{2+}_A \rightarrow Fe^{3+}_A + Cu^{2+}_B$. This reaction is thermodynamically favoured because of the greater preference of Cu^{2+} ions than Fe^{3+} ions to occupy B sites from a ligand-field stabilization energy standpoint [32]. Results obtained showed that the cubic-to-tetragonal transformation of the spinel decreased its percentage from 62 to 20.9%, while it did not affect the phase percentage of tenorite (38 %) and produced a new phase, hematite (40.2 %). Therefore, the cubic-to-tetragonal transformation of the spinel resulted in a segregation of the iron oxide from the spinel structure. This phenomenon was also described elsewhere [33,34].

CFNS600 exhibits the lowest spinel content compared to the other composites. In this case, hematite was the main crystalline phase with a crystallite size of 71.3 nm that may affect its electrocatalytic response towards ORR.

To study the surface composition and to distinguish the different oxidation states and coordination numbers of the cations, the CFNS composites were characterized by XPS. The XPS spectra of the samples CFNS, CFNS200, CFNS400, and CFNS600 are displayed in Figure S4, and the results are compiled in Table 2. All samples showed two Fe $2p_{3/2}$ peaks at BEs of 709.8 eV and 711.3 eV, assigned to Fe^{3+} cations in more than one coordination environment, i.e., B sites at lower BE and A sites at higher BE [29,35,36]. The peak at around 711 eV in CFNS600 is also due to Fe^{3+} in octahedral sites of hematite[37]. So, the XPS Fe profile of this sample will not be discussed with the rest of CFNS series. Based on the area under each peak of the as-prepared CFNS sample, it has 35 % of Fe^{3+} ions in octahedral surface sites and 65 % of Fe^{3+} ions in tetrahedral surface sites. The percentage of these peaks decreased (up to 32 %) and increased (up to 68 %), respectively, when calcination temperature increased up to 400 ºC (Table 2), indicating that inverse spinel formation was favoured in that way, supporting the above exchange reaction.

Table 1. Crystal phases, phase percentage and average crystallite size for CFNS composites obtained from the XRD patterns.

Sample	Crystal phase	Phase percentage	Crystallite size (nm)
CFNS	Cubic spinel (c-$CuFe_2O_4$)	67.5	7.8
	Cuprite (Cu_2O)	17.1	9.8
	Copper	15.4	90.0
CFNS200	Cubic spinel (c-$CuFe_2O_4$)	66.7	7.9
	Cuprite (Cu_2O)	20.1	13.8
	Copper	13.2	110.1
CFNS400	Cubic spinel (c-$CuFe_2O_4$)	62.0	8.3
	Tenorite (CuO)	38.0	24.1
CFNS600	Tetragonal spinel (t-$CuFe_2O_4$)	20.9	10.2
	Tenorite (CuO)	38.9	34.7
	Hematite (Fe_2O_3)	40.2	71.3

Table 2. Binding energy of the main XPS peaks with the quantification and the ratio of both cations for the CFNS composites

Sample	Fe $2p_{3/2}$/ eV	Fe_{at}/ %	Cu $2p_{3/2}$/ eV	Cu_{at}/ %	Cu/Fe
CFNS	709.8 (35) 711.3 (65)	24.7	932.3 (78) 933.5 (22)	5.4	0.22
CFNS200	709.8 (33) 711.3 (67)	24.4	932.3 (41) 933.5 (59)	5.0	0.21
CFNS400	709.8 (32) 711.2 (68)	23.5	933.6 (100)	4.7	0.20
CFNS600	709.7 (30) 711.2 (70)	20.7	933.8 (100)	6.8	0.33

CFNS and CFNS200 showed two Cu $2p_{3/2}$ peaks at 932.3 and 933.5 eV, assigned to reduced copper species (Cu^0/Cu^+) and Cu^{2+}, respectively [38,39]. The Cu^+ surface concentration was lower on CFNS200 than on CFNS consistent with the larger crystallite size of Cu_2O measured by XRD in the former. Finally, CFNS400 and CFNS600 showed a single peak at 933.6-933.8 eV, corresponding to Cu^{2+}.

3.2.Electrochemical characterization

The different calcination treatment on the CFNS composites, which results in different physicochemical properties, is expected to influence the electrochemical properties, which in turn has an effect on the electrocatalytic activity towards ORR. Firstly, the CFNS materials were characterized by cyclic voltammetry in a saturated atmosphere of N_2 or O_2. Then, the electroactivity of the materials towards ORR was studied using an RRDE. The results were compared to those obtained for the CFNS/Vulcan materials to understand the effect of the carbon support in the ORR.

3.2.1. Unsupported CFNS-based materials

The CFNS materials exhibit different electrochemical behaviour depending on the calcination temperature. Figure 2 displays the steady cyclic voltammograms of the different metal oxides in 0.1 M KOH in N_2-saturated atmosphere. It can be observed that the materials have different voltammetric profiles; however, in all cases, anodic overlapped processes between 0.4-0.6 V, which could be related to the oxidation of copper species, are observed. The corresponding reduction peaks shifted from -0.05 V to -0.1V. The assignment is a bit difficult due to the overlapped processes. In the case of CFNS200, two processes can be vaguely distinguished in the positive-going scan at 0.4V and 0.6V, which can be assigned to $Cu^0 \rightarrow Cu^+$ and $Cu^+ \rightarrow Cu^{2+}$, respectively [35]. Regarding CFNS400, it exhibited a similar electrochemical response to that of CFNS200, although these redox processes are more defined. This is in agreement with the presence of Cu(II) forming tenorite, as deduced from the XRD patterns. However, CFN600 sample exhibits a cathodic peak which may be mainly related to the reduction of Cu(II), but the counterprocess in the anodic scan decreases. This might be attributed to the low stability of Cu species in the structure of CFNS600, which could be related to the partial segregation of the iron oxide from the spinel structure.

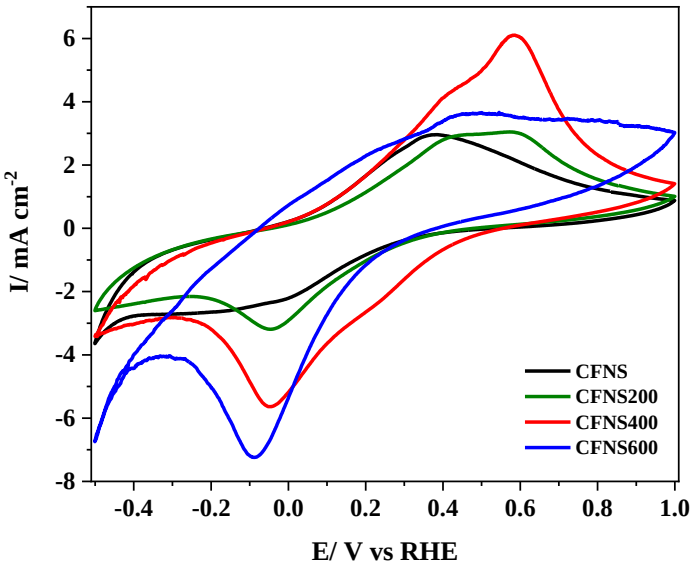

Figure 2. Cyclic voltammograms of CFNS composites deposited on glassy carbon substrates in 0.1 M KOH medium saturated with N_2. Scan rate: 50 mV s^{-1}.

3.2.2. Analysis of the electrocatalytic activity towards ORR

To assess the electrocatalytic performance of the CFNS-based materials towards ORR, linear sweep voltammetry (LSV) curves were obtained by the RRDE in 0.1M KOH medium saturated in oxygen. Figure 3a shows the LSV curves for the CFNS-based materials, and a two-wave electrocatalytic process can be distinguished, the first step starts at around 0.7 V with the reduction of oxygen, and the second one appears at around 0.4 V, which involves the reduction of oxygen and peroxide. Figure 3b displays the obtained number of electrons and it can be noted that at 0.7 V the number of electrons varies in a wide range for the different samples (from 2.7-3.4), showing the lowest number of electrons the sample calcined at 600 ºC, and the highest the sample heat-treated at 200 ºC.

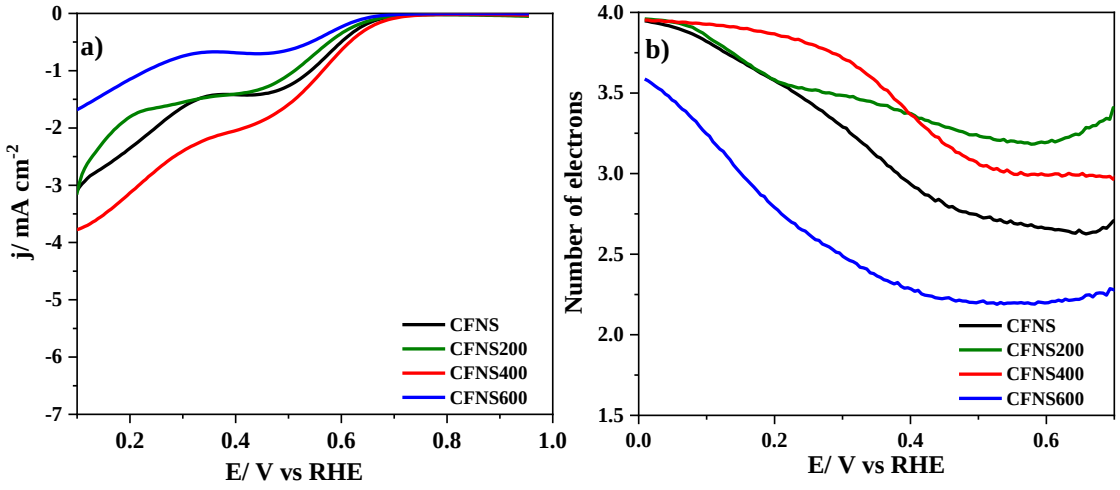

Figure 3. a) Linear sweep voltammograms recorded at 1600 rpm for CFNS composites in O_2-saturated 0.1 M KOH solution. Scan rate: 5 mV s^{-1}; **b)** Electron transfer numbers calculated from the current measured at the ring using Eq. 4.

Table 3 summarizes the electrochemical parameters obtained for the CFNS-based samples. The slightly different electrocatalytic response of CFNS-based materials can be ascribed to the different crystal structures that formed the samples, which have different activities towards ORR. Among the copper-containing structures, CuO is the most active because Cu^{2+} is an active site for ORR, whereas the Cu_2O is not a good electrocatalyst due to its poor conductivity as was reported [36,38]. Thus, the presence of a cubic spinel and tenorite phases in CFNS400-based materials (Table 2) could explain its better ORR performance, showing a higher E_{onset} and limiting current density. The ORR mechanism suggested for spinel structures is a multi-step process that involves: (i) the oxygen adsorption; (ii) the surface peroxide formation; (iii) surface oxide formation; and (iv) surface hydroxide regeneration, resulting in the total reduction of oxygen to hydroxide [17,40]. Regarding the Fe_2O_3 crystal structure, which is the main structure in the CFNS600-based material, it was reported as an active catalyst in the ORR through a mixed two-electron and four-electron pathways, but in this case, the activity might be limited by the large crystallite size, and then the low electrochemical surface area [39,41]. The great difference in the ORR performance of the CFNS600 material compared to the other CFNS samples, which has a much lower activity, seems to be related to the different crystal structures and their concentration. In this sample, $CuFe_2O_4$, which is tetragonal, might

influence in the ORR activity because a cubic structure provides a higher number of catalytic sites than the tetragonal structure, which can interact properly with O_2 since most of Fe^{3+} are in octahedral sites [17,19]. Moreover, the samples having spinel with cubic structure have higher BET surface area and smaller particles size compared to CFNS600, what favour the electrode/electrolyte contact that increases the electron transfer, resulting in a better ORR performance [42].

Table 3. Onset potential, number of electrons, limiting current density and Tafel slope obtained for the ORR reaction at CFNS-based samples.

Sample	E_{onset} / V (at -0.10 mA cm^{-2})	n_{e^-} (at 0.4 V vs RHE)	j_{lim} / mA cm^{-2} (at 0.4 V)	Tafel slope / mV dec^{-1}
CFNS	0.67	2.95	-1.42	94
CFNS200	0.67	3.38	-1.41	115
CFNS400	0.69	3.38	-2.05	101
CFNS600	0.64	2.29	-0.68	100

Regarding the Tafel slope values obtained from the Figure S5a, the CFNS generally have a combination of two steps as the rate-determining step, i.e., the oxygen adsorption and the surface peroxide formation [43], revealing that CFNS200 show inferior kinetics in terms of electron transfer. Despite the large number of electrons by which the ORR occurs on the CFNS200, it has the higher Tafel slope value related to the rate-determining step of the surface peroxide formation. However, it can be concluded that all the samples show a poor electrocatalytic activity to this reaction.

3.2.3. CFNS mixed with carbon black

Previous studies based on metal oxide materials have claimed that the synergistic effect between metal oxides and carbon supports enhances the performance towards ORR [44]. Moreover, the metal oxide/carbon material ratio is very important to achieve a good electroactive response of the resulting composites. Furthermore, previous studies have reported that the optimum metal oxide/carbon material ratio is equal to 1:1 [22,45]. The BET surface area of all the composites is around 110 m^2 g^{-1} since it is determined by the 50% of Vulcan present in the composite materials.

Figure 4 shows the steady cyclic voltammograms of the materials in an N_2-saturated atmosphere and we can observe very important differences related to the increase of the pseudocapacitance as a result of the presence of Vulcan, which increases the electrical conductivity of the composites and the accessible surface area of the oxide particles[9]. Thus, the redox processes of the metal oxides are much more clearly observed. These redox processes are very much dependent on the metal oxide particle size and sintering degree. Within the potential region studied, the carbon support has no redox activity and it only shows double-layer charging processes. The composites show redox processes associated with Cu species. In the anodic sweep, we can observe different peaks associated to Cu species; the peak at 0.6 V is related to the Cu^0/Cu^+ redox couple, whereas the peak at 0.9 V corresponds to two different redox couples Cu^0/Cu^{2+} or Cu^+/Cu^{2+}. In the cathodic sweep, the counterpart redox reactions can be observed: the redox couple of Cu^{2+}/Cu^+ is at 0.55 V and the peak at 0.3 is related to the Cu^+/Cu^0 [46,47]. However, the redox processes related to the iron species at lower potentials can be observed mainly in the samples CFNS/ Vulcan and CFNS200/ Vulcan [48]. The CFNS400/ Vulcan and CFNS600/Vulcan materials do not display any anodic peak due to iron species because the cathodic peak is shifted towards lower potentials with increasing the calcination temperature.

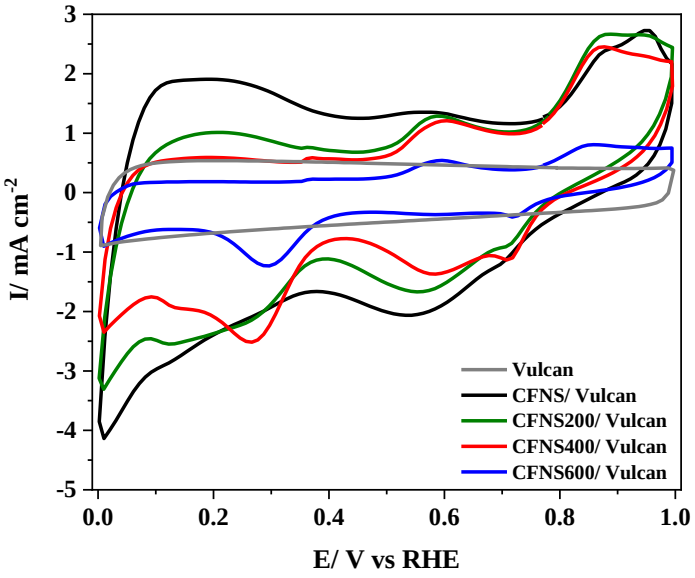

Figure 4. Cyclic voltammograms of CFNS/ Vulcan materials deposited on glassy carbon substrates in 0.1 M KOH medium saturated with N_2. Scan rate: 50 mV s^{-1}.

3.2.4. Analysis of the electroactivity of composites towards ORR

Figure 5 shows both LSV curves and the number of transferred electrons obtained for the CFNS/ Vulcan composites and Pt/ Vulcan material, used as reference electrocatalyst, towards ORR. Figure 5a depicts the LSV curves of all composites, Vulcan and Pt/ Vulcan samples to compare the electrochemical behaviours. As it is well-known from the literature [49], the Pt/ Vulcan electrocatalyst exhibits the best response towards ORR in terms of onset potential and current density. For the CFNS-based composites, an improvement in the limiting current density is observed and, in most of the cases, a clear improvement in onset potential occurs. Besides, Figure 5b reveals in the Pt/ Vulcan material, the ORR mainly occurs through a 4-electron pathway, whereas for all CFNS-based composites is close to 4-electron pathway, which indicates a low amount of hydrogen peroxide formation (Figure S6), except for sample CFNS600/ Vulcan at more positive potentials. Taking into account the above mentioned results and those obtained for the CFNS samples without mixing with Vulcan, it can be concluded that there is a synergistic effect between both materials, which enhances the performance of ORR. CFNS/Vulcan and CFNS400/ Vulcan exhibit better performance compared to the other CFNS-based composites due to the differences in the crystal structure and composition. In the first case, cubic spinel is the main phase and in the second cubic spinel as well as tenorite are present in the material and both are the most active for ORR.

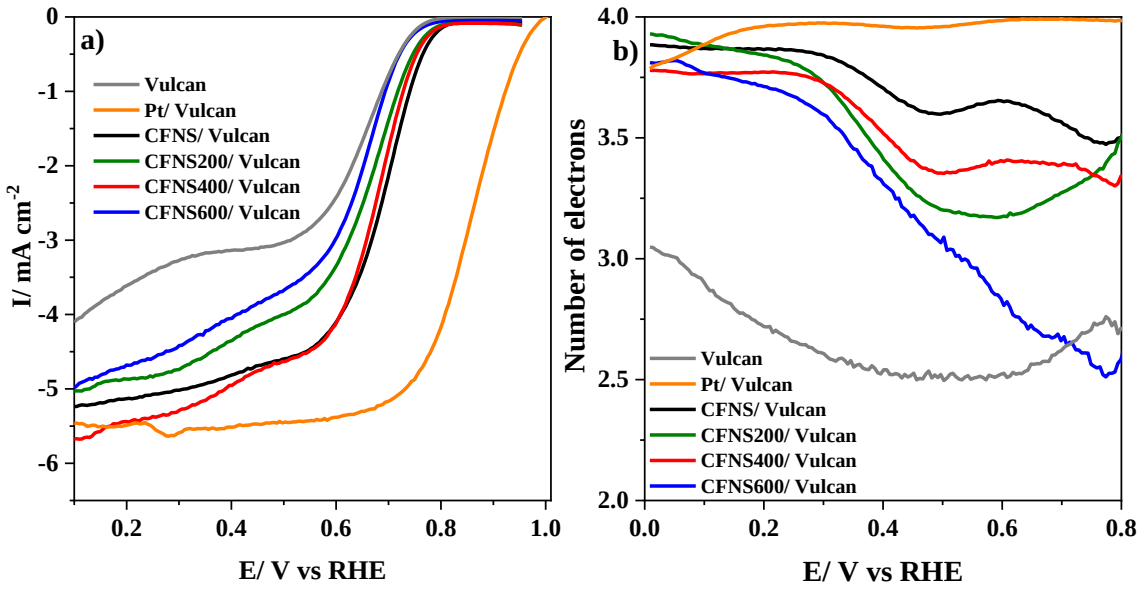

Figure 5. a) Linear sweep voltammograms recorded at 1600 rpm for CFNS/ Vulcan materials in O_2-saturated 0.1 M KOH solution. Scan rate: 5 mV s^{-1}; **b)** Electron transfer number calculated from the current measured at the ring using Eq. 4.

The electrochemical parameters obtained for the CFNS/ Vulcan composites are collected in Table 4. Generally, the composites display better performance towards ORR, except for CFNS600/ Vulcan material whose electroactivity is lower than the other samples. It can be observed that all the electrochemical parameters are improved with respect to the components alone (Table 3 and Table 4), due to both the increase in electrical conductivity by Vulcan addition and a synergistic effect of both components. The electrical conductivity of CFNS samples measured by the four-point probe method showed its poor electrical conductivity values ($<10^{-3}$ S cm^{-1}), which were increased up to electrical conductivity values ranging from 1.4 to 2.1 S cm^{-1} after the addition of Vulcan.

Figure 6 shows the relation between the catalytic performance of the CFNS/ Vulcan composites and the calcination temperature used to prepare the CFNS-based material. The sample without the post-calcination treatment (CFNS/ Vulcan) exhibits a good performance in ORR due to the major presence of c-$CuFe_2O_4$ that is the crystal structure more active towards ORR. The sample CFNS200/ Vulcan, despite having the same crystal structures and percentages, exhibits lower catalytic performance because its smaller BET surface area limits the interaction between it and Vulcan. However, the catalytic performance of CFNS400/ Vulcan improves due to the copper present in the composite in the form of CuO that is catalytically active for ORR. Regarding CFNS600/ Vulcan composite, it displays the worst catalytic performance in ORR because c-$CuFe_2O_4$ is transformed into t-$CuFe_2O_4$, being t-$CuFe_2O_4$ less active than the cubic structure. Moreover, although Fe_2O_3 and CuO are present in the material and are active for ORR, the larger crystal size and lower surface area, limit its catalytic performance. Figure 6 shows that the number of electrons does not vary significantly with the temperature of calcination.

The role of Vulcan in the as-synthesized composites, apart from enhancing the electrical conductivity between the particles of the oxides that results in a better performance, can also be due to a co-catalytic effect. It has been reported that Vulcan may act as co-catalyst because the oxygen molecule can be first reduced by the carbon material to peroxide by

a 2-electron pathway which can then be further reduced over the adjacent metal oxide species to hydroxide, increasing the overall catalytic activity [11,50].

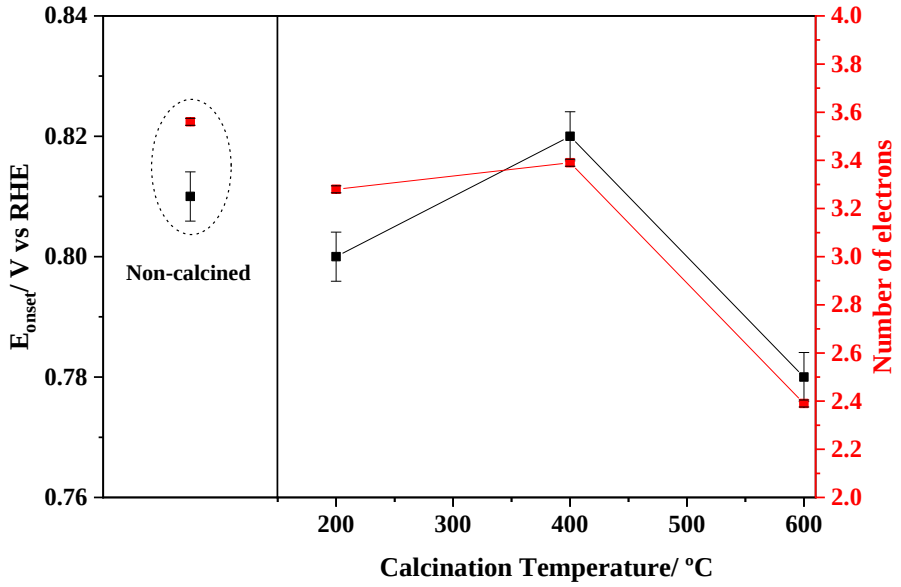

Figure 6. Change in the E_{onset} and the number of electrons of the CFNS/Vulcan composites with the calcination temperature of the oxide materials.

The values of the Tafel slope of the CFNS/Vulcan composites calculated from Figure S5b are lower compared to the metal oxides (Table 3 and Table 4), demonstrating an enhancement in the kinetics of the electron transfer when the metal oxide materials are mixed with the conductive carbon material. The CFNS/ Vulcan composite shows the lowest Tafel slope value, and it increases slightly in the calcined samples, although all of them have the same Tafel slope, demonstrating that the calcination temperature slightly affects the kinetics of the reactions.

Table 4. Onset potential, number of electrons, limiting current density and Tafel slope obtained for the ORR reaction at CFNS/ Vulcan composites.

Sample	E_{onset} / V (at -0.10 mA cm^{-2})	n_{e^-} (at 0.7 V vs RHE)	j_{lim} / mA cm^{-2} (at 0.4 V)	Tafel slope / mV dec^{-1}
CFNS/ Vulcan	0.81	3.71	-4.82	70
CFNS200/ Vulcan	0.80	3.43	-4.36	81
CFNS400/ Vulcan	0.82	3.53	-4.95	80
CFNS600/ Vulcan	0.78	3.32	-4.05	81
Pt/ Vulcan	0.98	3.99	-5.51	60
Vulcan support	0.77	2.53	-3.14	62

The stability of the CFNS400/ Vulcan composite was studied by a chronoamperometric technique using the RRDE at 1600 rpm in O_2-saturated electrolyte at a constant potential of 0.5 V [51]. The performance of the composite material was compared with the commercial 20% Pt/ Vulcan sample (Figure 7). After 3 h at 0.5 V, methanol was added into the cell until 1.0 M concentration was reached. As it was expected, the 20% Pt/Vulcan catalyst shows a current retention close to the 95% after 3 h, but when methanol is added the recorded current drops to zero, revealing the poisoning of the catalytic active sites. The CFNS400/ Vulcan composite shows a slight decrease of the initial activity followed by a stabilization of the current density after 130 min, reaching a current retention of 90%. The composite displays much better methanol tolerance maintaining the activity. From the results of this test along with its electrocatalytic performance, it can be concluded that the CFNS400/ Vulcan composite can be a promising alternative to the platinum-based electrocatalysts for ORR in alkaline medium.

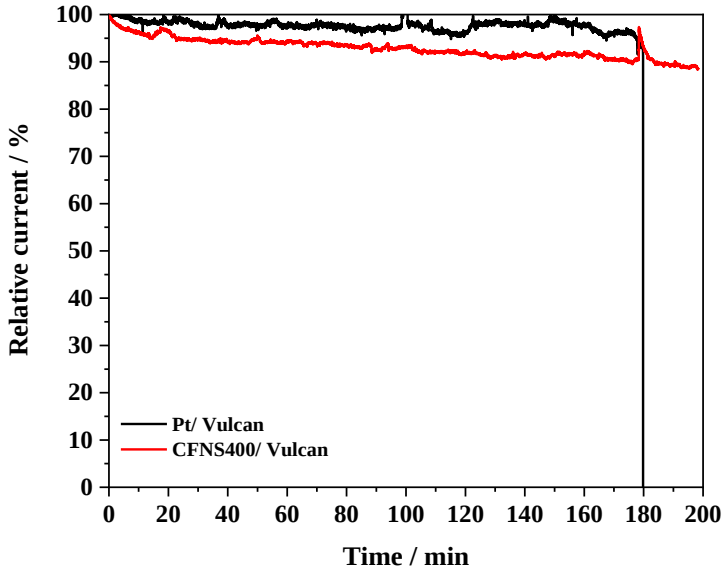

Figure 7. Comparative stability test for CFNS400/Vulcan and 20% Pt/Vulcan carried out at 0.5 V and 1600 rpm in O_2-saturated 0.1 M KOH and 25 ºC. Methanol was added 180 min after launching the experiment.

4. Conclusions

The CFNS materials synthesized by a solvothermal method displayed different crystal structure depending on the post-calcination temperature. CFNS and CFNS200 were composed of c-$CuFe_2O_4$, Cu_2O and Cu crystal phases. Cuprite (Cu_2O) and metallic copper were oxidized to tenorite (CuO) as the calcination temperature increased over 400 ºC, whereas the c-$CuFe_2O_4$ phase changed to t-$CuFe_2O_4$ phase and a new phase of Fe_2O_3 was observed at a calcination temperature of 600 ºC.

The CFNS materials showed a poor performance in ORR because of their low electrical conductivity. Moreover, the catalytic response was influenced by the crystal phases and concentration; thus, the samples containing c-$CuFe_2O_4$ and CuO are the most active for ORR. The CFNS600 sample exhibited the lowest catalytic response because of the formation of t-$CuFe_2O_4$, with lower activity, and the lowest surface area of the material could also affect in the ORR performance.

The CFNS/ Vulcan composites showed better catalytic response in ORR compared to those of CFNS samples, which is related to the enhancement in the electrical conductivity of the CFNS composites together with a synergistic effect between both materials that improve the catalytic activity. Moreover, the carbon support can act as co-catalyst

producing hydrogen peroxide that can be further reduced on the metal oxide phase. In any case, the best catalyst is that containing c-$CuFe_2O_4$ and CuO phases which are the most active for this reaction. Thus, among investigated CFNS/ Vulcan-based electrocatalysts, CFNS400/ Vulcan exhibited the best catalytic activity, good stability and resistance to the chemical poisoning.

Conflicts of interest

There are no conflicts to declare.

Acknowledgements

The authors (E.M., J.X.F.-L., D.S.-T.) thank MICINN (PID2019-105923RB-I00) for the financial support. J.X.F.-L. gratefully acknowledges MINECO for the financial support through an FPI contract (BES-2017-081598). D.S.-T. thanks MICINN for the "Juan de la Cierva" contract (IJCI-2016-27636).

References

1 N. Abas, A. Kalair and N. Khan, *Futures*, 2015, **69**, 31–49.

2 D. R. Dekel, *J. Power Sources*, 2018, **375**, 158–169.

3 D. Banham and S. Ye, *ACS Energy Lett.*, 2017, **2**, 629–638.

4 N. M. Marković, T. J. Schmidt, V. Stamenković and P. N. Ross, *Fuel Cells*, 2001, **1**, 105–116.

5 G. R. Xu, J. J. Hui, T. Huang, Y. Chen and J. M. Lee, *J. Power Sources*, 2015, **285**, 393–399.

6 J. Quílez-Bermejo, E. Morallón and D. Cazorla-Amorós, *Chem. Commun.*, 2018, **54**, 4441–4444.

7 D. A. Kuznetsov, B. Han, Y. Yu, R. R. Rao, J. Hwang, Y. Román-Leshkov and Y. Shao-Horn, *Joule*, 2018, **2**, 225–244.

8 M. Chen, J. Liu, W. Zhou, J. Lin and Z. Shen, *Sci. Rep.*, 2015, **5**, 1–10.

9 G. Kéranguéven, S. Royer and E. Savinova, *Electrochem. commun.*, 2015, **50**, 28–31.

10 G. B. Kaufman, *J. Chem. Educ.*, 1993, **70**, A279.

11 A. Samanta and C. R. Raj, *J. Electroanal. Chem.*, 2019, **847**, 113183.

12 V. D. Silva, L. S. Ferreira, T. A. Simões, E. S. Medeiros and D. A. Macedo, *J. Colloid Interface Sci.*, 2019, **540**, 59–65.

13 Y. Liu, Z. Niu, Y. Lu, L. Zhang and K. Yan, *J. Alloys Compd.*, 2018, **735**, 654–659.

14 H. Zhu, S. Zhang, Y. X. Huang, L. Wu and S. Sun, *Nano Lett.*, 2013, **13**, 2947–2951.

15 W. Bian, Z. Yang, P. Strasser and R. Yang, *J. Power Sources*, 2014, **250**, 196–203.

16 J. Li, J. Chen, H. Wan, J. Xiao, Y. Tang, M. Liu and H. Wang, *Appl. Catal. B Environ.*, 2019, **242**, 209–217.

17 C. Li, X. Han, F. Cheng, Y. Hu, C. Chen and J. Chen, *Nat. Commun.*, 2015, **6**, 1–8.

18 H. Liu, X. Zhu, M. Li, Q. Tang, G. Sun and W. Yang, *Electrochim. Acta*, 2014, **144**, 31–41.

19 E. Lee, J. H. Jang and Y. U. Kwon, *J. Power Sources*, 2015, **273**, 735–741.

20 A. Samanta and C. R. Raj, *J. Electroanal. Chem.*, 2019, **847**, 113183.

21 J. Liu, X. Jin, W. Song, F. Wang, N. Wang and Y. Song, *Chinese J. Catal.*, 2014, **35**, 1173–1188.

22 T. Li, J. Liu, X. Jin, F. Wang and Y. Song, *Electrochim. Acta*, 2016, **198**, 115–126.

23 C. Moreno-Castilla, M. V. López-Ramón, M. ángeles Fontecha-Cámara, M. A. Álvarez and L. Mateus, *Nanomaterials*, 2019, **9**, 901.

24 H. Deng, H. Chen and H. Li, *Mater. Chem. Phys.*, 2007, **101**, 509–513.

25 J. Feng, L. Su, Y. Ma, C. Ren, Q. Guo and X. Chen, *Chem. Eng. J.*, 2013, **221**, 16–24.

26 Y. Xue, H. Miao, S. Sun, Q. Wang, S. Li and Z. Liu, *J. Power Sources*, 2017, **342**, 192–201.

27 M. Thommes, K. Kaneko, A. V. Neimark, J. P. Olivier, F. Rodriguez-Reinoso, J.

Rouquerol and K. S. W. Sing, *Pure Appl. Chem.*, 2015, **87**, 1051–1069.

28 V. A. M. Brabers and J. Klerk, *Thermochim. Acta*, 1977, **18**, 287–294.

29 I. Nedkov, R. E. Vandenberghe, T. Marinova, P. Thailhades, T. Merodiiska and I. Avramova, *Appl. Surf. Sci.*, 2006, **253**, 2589–2596.

30 Z. Xiao, S. Jin, X. Wang, W. Li, J. Wang and C. Liang, *J. Mater. Chem.*, 2012, **22**, 16598.

31 K. Faungnawakij, N. Shimoda, T. Fukunaga, R. Kikuchi and K. Eguchi, *Appl. Catal. B Environ.*, 2009, **92**, 341–350.

32 .E. Huheey, E.A. Keiter, R.L. Keiter, in: Inorganic Chemistry: Principles of Structure and Reactivity, Fourth ed., Harper Collins, New York, 1993.

33 P. Laokul, V. Amornkitbamrung, S. Seraphin and S. Maensiri, *Curr. Appl. Phys.*, 2011, **11**, 101–108.

34 R. S. Yadav, I. Kuřitka, J. Vilcakova, J. Havlica, J. Masilko, L. Kalina, J. Tkacz, M. Hajdúchová and V. Enev, *J. Mater. Sci. Mater. Electron.*, 2017, **28**, 6245–6261.

35 U. Sander, H-H. Strehblow and J. K. Dohrmann, *Phys. Chem. A*, 1981, **839**, 447–450.

36 J. Yu, T. Huang, Z. Jiang, M. Sun and C. Tang, *Molecules*, , DOI:10.3390/molecules24030441.

37 X. Shi, B. Chu, F. Wang, X. Wei, L. Teng, M. Fan, B. Li, L. Dong and L. Dong, *ACS Appl. Mater. Interfaces*, 2018, **10**, 40509–40522.

38 C. Goswami, K. K. Hazarika and P. Bharali, *Mater. Sci. Energy Technol.*, 2018, **1**, 117–128.

39 Y. Fu, J. Wang, H. Y. Yu, X. Li, H. Wang, J. H. Tian and R. Yang, *Int. J. Hydrogen Energy*, 2017, **42**, 20711–20719.

40 J. Suntivich, H. A. Gasteiger, N. Yabuuchi, H. Nakanishi, J. B. Goodenough and Y. Shao-Horn, *Nat. Chem.*, 2011, **3**, 546–550.

41 Z. Xiao, F. Hou, Y. Li, R. Zhang, G. Shen, L. Wang, X. Zhang, Q. Wang and G. Li, *Chem. Eng. Sci.*, 2019, **207**, 235–246.

42 Z. Xing, Z. Ju, J. Yang, H. Xu and Y. Qian, *Electrochim. Acta*, 2013, **102**, 51–57.

43 T. Shinagawa, A. T. Garcia-Esparza and K. Takanabe, *Sci. Rep.*, 2015, **5**, 13801.

44 Y. Zhu, W. Zhou and Z. Shao, *Small*, 2017, **13**, 1603793.

45 X. Chen, S. Chen, B. Nan, F. Jia, Z. Lu and H. Deng, *Ionics (Kiel).*, 2017, **23**, 2241–2250.

46 A. Ashok, A. Kumar, M. A. Matin and F. Tarlochan, *J. Electroanal. Chem.*, 2019, **844**, 66–77.

47 A. A. Ensafi, E. Heydari-Soureshjani, S. S. Afiyuni and B. Rezaei, *Int. J. Hydrogen Energy*, 2019, **44**, 16497–16506.

48 J. Shao, X. Li, Y. Ding, Z. Wan, H. Liu, J. Yun, Y. Liu, Q. Qu and H. Zheng, *Electrochem. commun.*, 2014, **40**, 9–12.

49 C. Cui, L. Gan, M. Heggen, S. Rudi and P. Strasser, *Nat. Mater.*, 2013, **12**, 765–771.

50 J. T. Mefford, A. A. Kurilovich, J. Saunders, W. G. Hardin, A. M. Abakumov, R. P. Forslund, A. Bonnefont, S. Dai, K. P. Johnston and K. J. Stevenson, *Phys. Chem. Chem. Phys.*, 2019, **21**, 3327–3338.

51 K. Liu, J. Li, Q. Wang, X. Wang, D. Qian, J. Jiang, J. Li and Z. Chen, *J. Alloys Compd.*, 2017, **725**, 260–269.